Finite-Element Model for Modified Boussinesq Equations. II: Applications to Nonlinear Harbor Oscillations

Seung-Buhm Woo[1] and Philip L.-F. Liu[2]

Abstract: The finite-element model for modified Boussinesq equations developed in Part I of this paper is used to study harbor resonance problems. The internal wavemaker technique is implemented on an unstructured finite-element mesh, and a sponge layer is used as an open boundary condition. Both linear and nonlinear harbor oscillations in rectangular and circular basins are examined, and experimental measurements and analytical solutions are used to validate the model. Finally, the wavelet transform is employed to analyze transient features of the nonlinear resonance problem.

DOI: 10.1061/(ASCE)0733-950X(2004)130:1(17)

CE Database subject headings: Boussinesq equations; Finite element method; Wave generation; Harbors; Resonance; Nonlinear response.

Introduction

Harbor resonance is the phenomenon of trapping and amplification of wave energy inside a semienclosed water body, such as a harbor or bay. If wave motions inside a harbor are forced to occur at one or more of the natural frequencies of the harbor, which depend on the harbor configuration, the amplitudes of harbor oscillations will become large and could create unacceptable vessel movements and excessive mooring forces, leading to the breaking of mooring lines. In designing a new harbor or modifying an existing one, it is essential to have a good understanding of the natural frequencies of the harbor and the possible sources of forcing for harbor resonance. Moreover, a model, either numerical or physical, should be used to examine the temporal and spatial variations of wave amplitudes inside the proposed harbor under design wave conditions.

For a simple harbor geometry with constant depth, the natural frequencies and corresponding free-surface oscillations can be predicted analytically. However, for more complex harbor geometry, transient excitations, and cases where nonlinear effects are important, the harbor response can be determined only from experiments conducted in a hydraulic model or with a numerical model. Although the usefulness of conducting a hydraulic model study should never be underestimated, there are several limitations. First, it is costly to construct and modify the hydraulic model to collect data for a long duration with a fine spatial resolution, and second, scaling the hydraulic model is also difficult when both short waves and infragravity waves are of interest. Therefore, research efforts focused on the development of numerical models for calculating the harbor oscillations induced by nonlinear transient waves are essential.

Several existing numerical models could be used to calculate harbor oscillations. Using the linear mild-slope equation, several research groups have developed various finite-element models (FEM), for example, Chen and Mei (1974), Tsay and Liu (1983), Xu et al. (1996), Jeong (1999), and Panchang et al. (2000). These models calculate linear monochromatic wave oscillations in harbors of arbitrary configuration and variable bathymetry. The effects of bottom friction and boundary absorption (partial reflection) are usually included. These models, which use a hybrid element solution method that combines analytical (in the offshore area) and finite-element numerical (near and inside the harbor) solutions to determine harbor responses to small-amplitude waves with a single wave frequency, are an extension of the original model for linear shallow-water equations developed by Chen and Mei (1974).

Because of their simplicity, these models have been used for assessing design or modification of existing harbors [for example, Lillycrop et al. (1993); Panchang et al. (2000)]. However, the most serious drawback of these models is the limitation of using linear theory, since they cannot be used to investigate harbor oscillations induced by nonlinear transient waves.

Lepelletier (1980) developed an FEM for solving conventional Boussinesq equations (CBEs) [see also Lepelletier and Raichlen (1987)]. The model includes several dissipative effects, such as bottom friction and entrance losses, and a time-varying radiation condition at a finite distance from the harbor entrance is used to simulate open sea conditions. Since the model employs CBEs, the water depth must remain small relative to the wavelength in the entire domain of interest, including the offshore region. Therefore this model is not suitable for studying problems where incident waves consist of short wave components, which could be responsible for generating bound and free infragravity waves that could be resonated near and inside the harbor.

To include the short wave components, modified (or extended) Boussinesq equations (MBEs) have been intensively studied in recent years. Among these, Nwogu's (1993) MBEs have been widely used for various physical problems. The MBEs are applicable to waves whose lengths are about twice the water depth.

---

[1] Senior Researcher, Water Resources Research Dept., Korea Institute of Construction Technology, Gyeonggi-do, Korea.

[2] Professor, School of Civil and Environmental Engineering, Cornell Univ., Ithaca, NY 14853.

Note. Discussion open until June 1, 2004. Separate discussions must be submitted for individual papers. To extend the closing date by one month, a written request must be filed with the ASCE Managing Editor. The manuscript for this paper was submitted for review and possible publication on November 27, 2002; approved on June 9, 2003. This paper is part of the ***Journal of Waterway, Port, Coastal, and Ocean Engineering***, Vol. 130, No. 1, January 1, 2004. ©ASCE, ISSN 0733-950X/2004/1-17–28/$18.00.

In Part I of this paper, Woo and Liu (2004) developed an FEM for Nwogu's MBEs using the Galerkin method with linear elements. Auxiliary variables are introduced to reduce the third-order spatial derivatives in the governing equations to second order, and five matrix equations are constructed and solved using the predictor-corrector time-integration procedure with appropriate boundary conditions. The model has been verified by checking the numerical results with various known analytical solutions and experimental data.

This paper uses the FEM developed by Woo and Liu (2004) to study harbor oscillations, focusing especially on nonlinear super- and subharmonic generation through resonant interactions. Although several FDMs/FEMs exist for the MBEs (Nwogu 1993; Wei and Kirby 1995; Li et al. 1999; Walkley and Berzins 2002), to the writers' knowledge, computational results have not been published for the nonlinear harbor resonance problem. The main objective of this paper is to investigate the model performance for the nonlinear properties of harbor oscillation and compare it with existing theoretical/experimental data. An internal wavemaker is implemented inside the computational domain and a sponge layer is installed in the open ocean so that both incident wave generation and radiated waves are treated accurately.

Since the present FEM is a time domain model, the temporal variation of the physical system can be represented. It is interesting to examine the rate of energy transfer between different harmonic components in time. The wavelet transform technique is used to analyze the transient feature of the harbor resonance.

The next section describes the internal wavemaker embedded in an unstructured mesh. Then the section on linear oscillation first applies the model to the classical problem of linear resonance in a rectangular bay, and then, to test a more generally shaped harbor, studies the linear resonant responses of a circular harbor. The succeeding section on nonlinear oscillations first discusses resonant excitation in a rectangular bay and then presents wave-group-induced harbor resonance. We end the paper with some concluding remarks.

Wave Generation inside Domain

Proper treatment of incident wave generation and radiation of outgoing waves is critical to ensuring the accuracy of any harbor oscillation model. Within the framework of linear wave theory, the total wave field is the sum of incident waves and radiated waves, and therefore only the radiated wave field needs to be solved. For a nonlinear problem, however, the incident and radiated waves generated inside the computational domain cannot be separated. The problem of generating incident and radiating outgoing waves at the boundary at the same time becomes difficult but can be solved approximately by using a source function method; that is, the target waves are generated inside the computational domain, whereas the radiated waves are absorbed in the sponge layer located in the outer boundary of the domain.

Source Function Method

Under the linear theory assumption, Wei et al. (1999) presented a source function for the MBEs that relates source function magnitude to the target surface wave characteristics. The source term is added either to the continuity equation or to the momentum equations. This idea was implemented in their finite-difference model.

The same methodology is adopted in the present FEM. A source function F_w^η is added to the continuity equation. Assuming that the water depth is constant and the center of the source region is parallel to the y-axis, the source function can be written as follows (Wei et al. 1999):

$$F_w^\eta(x,y,t)=D\sin[k\sin(\theta_w)y-\omega t]\exp[-\gamma(x-x_w^s)^2] \tag{1}$$

where D=magnitude of source function; k=wave number; ω=wave frequency; γ=parameter associated with width of source function; x_w^s=x-coordinate of central location of source region; and θ_w=angle between propagation direction of the wave and the x-axis. For a monochromatic wave or single component of irregular waves, the source magnitude D can be determined by

$$D=\frac{2\eta_0(\omega^2-gC_6k^4h^3)\cos(\theta_w)}{\omega kI[1-C_5(kh)^2]} \tag{2}$$

where C_5, C_6=constants shown in Part I of this paper [Woo and Liu (2004)], that is, $C_5=\beta(\beta/2+1)$; $C_6=C_5+1/3$; $\beta=z_\alpha/h$; and I=integral constant given by

$$I=\sqrt{\frac{\pi}{\gamma}}\exp\left(-\frac{(k\cos\theta_w)^2}{4\gamma}\right) \tag{3}$$

Note that the width of the source function should be as narrow as possible, since the assumption of a linearized governing equation and constant water depth in the source region is made in derivation of the source function. On the other hand, enough grid points are needed in this region to generate the target waves. As a result, the choice of the γ value is decided by these two factors. The typical values of γ used in the present model are in the range of $80/\lambda^2-320/\lambda^2$ (λ=wavelength) corresponding to a source function width that is about 0.25–0.5 times the wavelength.

To apply the source function in the present FEM, it is approximated as a linear combination of shape functions and the nodal values of $F_w^\eta(x,y,t)$:

$$F_w^\eta(x,y,n\Delta t)\simeq\sum_{j=1}^{ND}\psi_j(x,y)\{F_w^\eta\}_j^n \tag{4}$$

where ND=total number of nodes; and $\psi_j(x,y)$=shape function. At each predictor step, the nodal values of $\{F_w^\eta\}_j^n$ are calculated and the global forcing vector is formulated. This global vector is used continuously in the iterative corrector step.

The region in which the source function is applied is decided based on the coordinate of the element centroid. Therefore the actual boundary of the source region on the unstructured mesh is irregular, as shown in Fig. 1. However, since the intensity of the source function is reduced exponentially in the source region, this irregularity does not affect the accuracy of the target wave generation.

To verify the accuracy of the source function method, we use the model to generate monochromatic waves. The target wave has an amplitude of 0.025 m, a wave length of 2.5 m, and a wave period of 1.27 s. The computational domain is $(x,y)\in[0,30]\times[0,0.1]$ m with a constant water depth of 1 m. The center of the source region is located at $x=15$, $y\in[0,0.1]$ m, and two sponge layers of 5 m width are placed at both ends of the domain. The computational domain is composed of 842 nodes and 1,120 elements over an unstructured triangular mesh so that the wave is resolved with approximately 20 nodes per wavelength. The time step of $\Delta t=0.025$ s is used, and the source region width is about 1 m.

Fig. 2 shows side-view snapshots of surface elevation at various times. The waves are generated at the source region and then propagate toward the ends of the domain. The sponge layer thick-

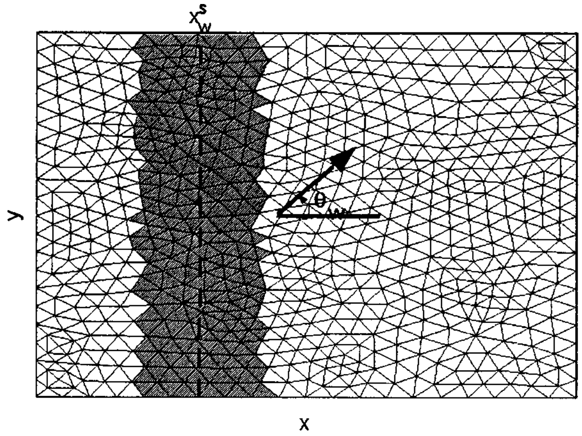

Fig. 1. Schematic diagram for source region and wave propagation direction

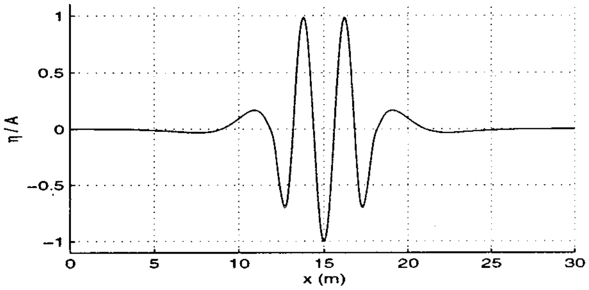

(a) t= 2.87 *sec*

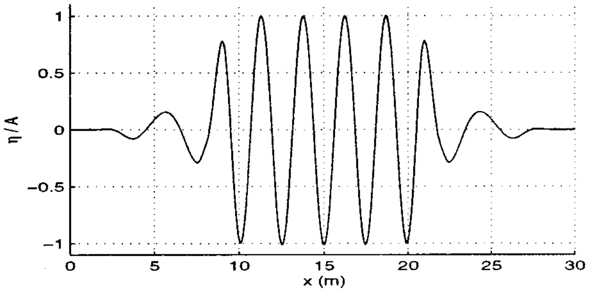

(b) t= 6.69 *sec*

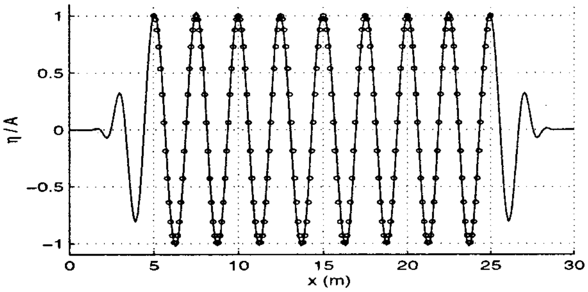

(c) t= 25.71 *sec*

Fig. 2. Side views of internally generated free-surface elevation of periodic wave

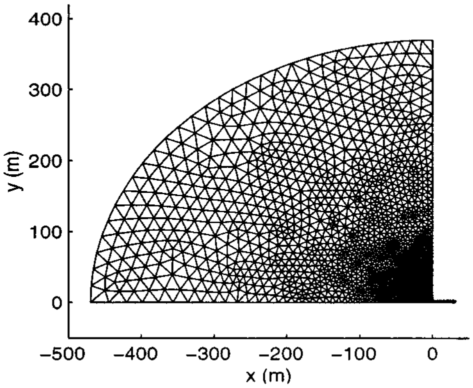

Fig. 3. Finite-element mesh for Ippen and Goda's (1963) experiment

ness is roughly 1.5 times the target wavelength, and sponge layers at both ends dissipate wave energy quite effectively. The model runs for 20 wave periods without any instability problem. The numerical solutions are compared with the analytic solution (which is plotted in circles) in Fig. 2(c). The agreement is quite good, indicating that both the internal generation of waves and the sponge layer are performing accurately.

Linear Oscillations

To evaluate the range of applicability of the present FEM, resonant responses of simply shaped harbors to periodic small-amplitude incident waves are first examined, and the simulation results are then compared with the existing experimental/theoretical data. Scaling of the domain size is usually used in this study to avoid the possible round-off error that can be generated at a very small element.

Resonance in Rectangular Bay

In this section, we consider the classical problem of resonance in a narrow rectangular harbor where the harbor width is much smaller than the harbor length. The wavelength of the incoming wave is much larger than the harbor length and the wave amplitude over water depth ratio is very small, so that the harbor response is linear.

Laboratory experiments were carried out by Ippen and Goda (1963) and Lee (1971). The dimensions used in the experiments are harbor width=0.0604 m, length=0.3111 m, and depth =0.2572 m. Laboratory data were collected at the center of the back wall of the harbor.

Fig. 3 shows the computational domain used in the present simulation. Due to symmetry, only the upper half of the domain is used for the computation so that the corresponding open boundary shape is a quarter circle. Note that the shape of the open boundary can be arbitrary due to the present combination of internal wavemaker and sponge layer. Compared with the FEM, based on a mild-slope equation in which the shape of the outer boundary should be circular so that a large amount of elements need to be used in the open ocean, the arbitrary shape of the open boundary could help reduce the computational cost considerably.

The computation was performed for a harbor with width=3.02 m, length=31.11 m, and depth=25.72 m, representing a 1:100 prototype for the experiment setup of Ippen and Goda (1963). The computational domain consists of 1,893 nodes and 3,592 triangu-

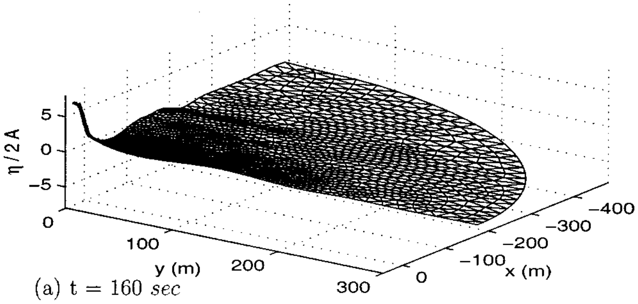

(a) t = 160 *sec*

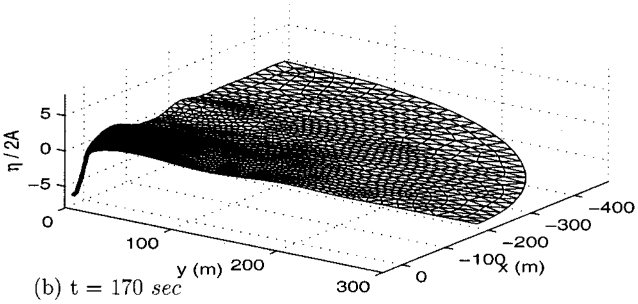

(b) t = 170 *sec*

Fig. 4. Snapshots of free-surface elevation for wave with wavelength of 148 m ($kL = 1.32$)

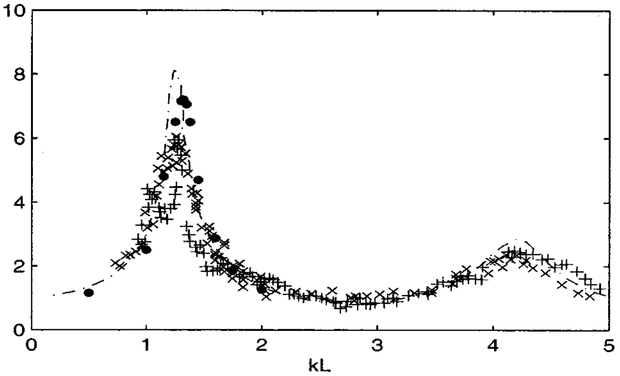

Fig. 5. Comparison of amplification factor at end of rectangular harbor: present numerical solution (●●●); Ippen and Goda's (1963) experiment (×××); Lee's experiment (+++); linear theoretical solution (—·—·—·—)

lar elements. The element size gradually increases toward Γ_W^E, which is the location of the open boundary, so that the length of the boundary element on Γ_W^E is around 20 times larger than the one near the harbor entrance. For the sponge layer, the center of the radiation ($\mathbf{x_c}$) is set at $(x,y) = (0,0)$, and the starting position of the sponge layer (Γ^S) is 180 m. The center of the internal wave-generation region is located at $x = -150$ m, and the area of the source region is $(x,y) \in [-165,-145] \times [0,150]$ m.

Fig. 4 shows snapshots of the free-surface elevation, which is normalized by the target wave height at different times. The incoming wavelength is 148 m, and the corresponding wave number parameter (kL), defined as the wave number times the harbor length, is 1.32. The laboratory experiments showed that the fundamental resonant mode occurs at this wave frequency. The incident wave amplitude is 0.33 m according to the experimental data, so that the nonlinearity is quite small ($a/h = 0.01$).

One of the most important factors in modeling harbor resonance problems is the absorption of radiated waves from the harbor. As is clearly seen, the sponge layer can effectively absorb radiated waves. Relatively large elements are used in the sponge layer (roughly 20 nodes in the sponge layer along $y = 0$), which reduces the large computational cost associated with the necessity for a relatively thick sponge layer (~1.5 times the wavelength).

Numerical simulations are performed for a range of kL values. The range covers the first resonant peak shown in the laboratory experiments. The numerical results indicate that the amplification factor at $kL = 1.32$, which is near the fundamental resonant frequency of the harbor, is around 7. On the other hand, Ippen and Goda (1963) showed that the linear theory overpredicts the amplification, that is, as almost 8. When $kL = 2$, the amplification factor is almost 1, and other cases show that the factor is between 1 and 5. The quasi-steady state can be reached within 10 wave periods in all cases, although there are modulation periods for some cases.

Fig. 5 compares the present numerical results with experimental data and linear theory. The agreement is quite good except near the resonant frequency, which could be due to the effect on the physical experiments of several energy dissipation mechanisms, such as entrance loss and bottom friction, which are not considered in the present numerical model.

Resonance in Circular Bay

To ensure that the present model can be applied to an arbitrarily shaped harbor, a simulation is performed for the harbor resonance in a circular harbor, and the simulation results are compared with the experimental data and analytic solutions (Lee 1971). Triangular unstructured elements are used to fit the circular boundary of the harbor, and the influence of the mesh quality on the efficiency and accuracy of numerical solutions is investigated.

Lee (1971) carried out laboratory experiments on harbor oscillations in a circular harbor with constant depth. In these experiments, the radius of the circular harbor R is 0.2286 m, and the constant depth is 0.3048 m. Two types of circular harbors were used, one with a 10° opening and the other with a 60° opening. The amplification factors at fixed points inside the harbor were measured as a function of wave-number parameter, defined as kR. One of the fixed points is located at the center of the harbor (denoted as P1), and the other is located at a distance of 0.213 m from the center with an angle of 45° (denoted as P2). The locations of P1 and P2 are indicated in Fig. 6(b).

The numerical model is applied only to the case with a 60° opening. Fig. 6 shows the computational domain used in the numerical simulation. The total number of elements is 8,358, and the total number of nodes is 4,302. In the simulation, a radius of 21 m and a depth of 28 m are used, representing a 1:91 prototype of the experiment setup. Since the incoming wave direction is normal to the harbor, only one-half of the domain is used.

The velocity gradient near the sharp edge at the tip of the harbor entrance is too high to be adequately represented by the linear interpolating functions adopted in the present model. To avoid this singularity problem, the sharp edge is rounded, and a mesh with a high resolution near the harbor mouth is employed [Fig. 6(b)].

The source region for the internal wavemaker is $(x,y) \in [-150,-130] \times [0,150]$ m. The incident wavelength varies from 386 to 87 m, corresponding to kR values from 0.35 to 1.5, respectively. For the location of the sponge layer, $\mathbf{x_c} = (0,0)$ and $\Gamma^S = 150$ m.

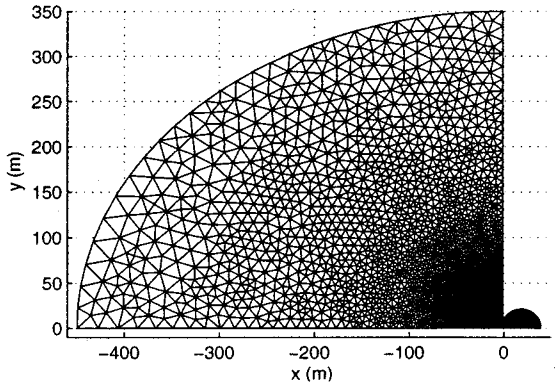

(a) Zoom-out view

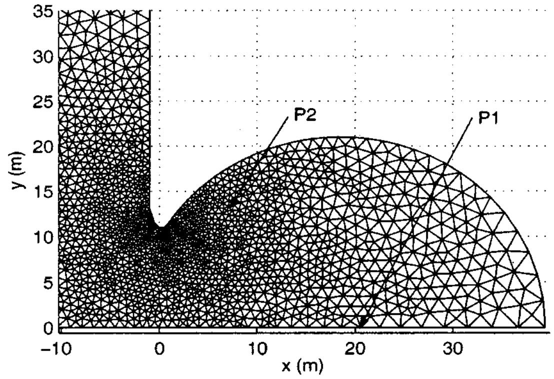

(b) Close view

Fig. 6. Finite-element mesh for Lee's (1971) experiment

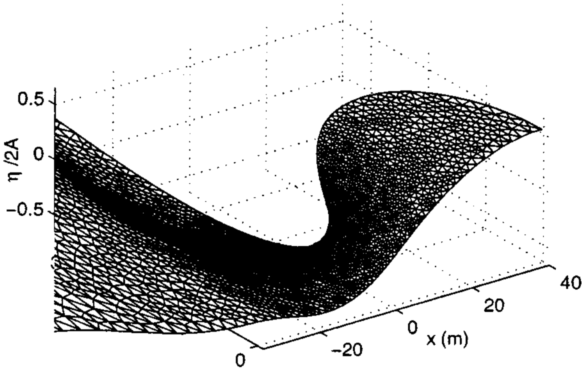

(a) t= 124.1 *sec*

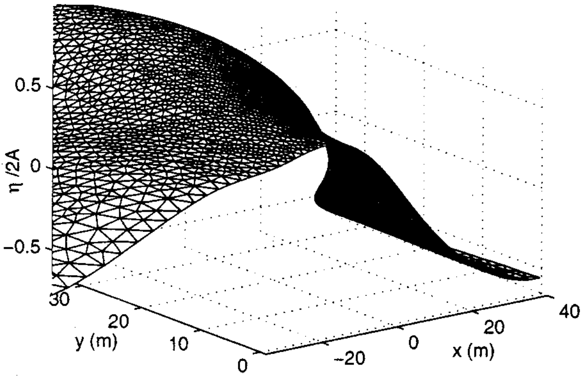

(b) t= 127.8 *sec*

Fig. 7. Snapshots of free-surface elevation for circular bay ($kR = 1.1$)

The snapshots of the free surface at its maximum and minimum elevation for $kR = 1.1$ is shown in Fig. 7. The whole free surface in the harbor moves up and down, showing behavior similar to that of the fundamental resonant mode. We remark here that if the original sharp edge boundary and a coarse mesh are used at the harbor mouth, noticeable high-frequency oscillations emerge, and a large number of iterations (sometimes more than 25) are required to obtain converged solutions. This is particularly true for $kR > 1.2$.

At the center point (P1), a quasi-steady state is reached within 4–5 wave periods. It takes a longer time to reach a quasi-steady state at P2, which is located closer to the harbor mouth. This pattern of reaching a quasi-steady state is similar for all waves tested in the present simulation.

Fig. 8 compares the present numerical solutions with Lee's (1971) experimental data and linear theoretical solutions and Jeong's (1999) numerical solution of the FEM based on mild-slope equations. At both P1 and P2, the general variation of the amplification factor is well represented by the present model. The amplification factor at the first resonant peak agrees well with the model results and experimental data. Jeong's (1999) FEM solution, where the partial reflective boundary condition is employed, agrees well with the measured data even when $kR > 1.0$. The present model does not include any energy dissipation mechanism, and as kR increases, the difference between the present solutions and the experimental data grows. This difference could also be caused by the boundary modification made at the harbor mouth.

Nonlinear Oscillations

Resonance Generation of Superharmonics

Rogers and Mei (1978), hereafter referred to as RM, investigated the nonlinear resonant excitation in a long and narrow bay. They used the CBEs inside the bay and the linear wave theory outside the bay so that the nonlinear problem inside the bay is decoupled from the problem in the ocean. The resulting 1D nonlinear, two-point boundary value problem inside the bay was solved numerically in the frequency domain. Experiments were also performed for a fixed frequency and three different bay lengths, which correspond to the first three resonant modes, respectively.

RM's numerical results for the second and third harmonics deviate significantly from experimental data. One reason for these differences could be that their experiments were performed in the intermediate depth condition, $\mu^2 = 0.257$, which is beyond the range of validity of the CBEs. Another reason could be that the assumption of linearizing the wave field outside the bay might not be accurate. Nevertheless, their work was the first rigorous study that investigated the importance of nonlinearity and dispersion in the harbor oscillation problem.

The present numerical model provides two important improvements to RM's approach. First, the governing equations adopted here provide a wider range of validity than the CBEs so that the dispersion parameter for RM's experiments is within the accuracy of the present model. Second, the nonlinear theory is applied to the whole domain.

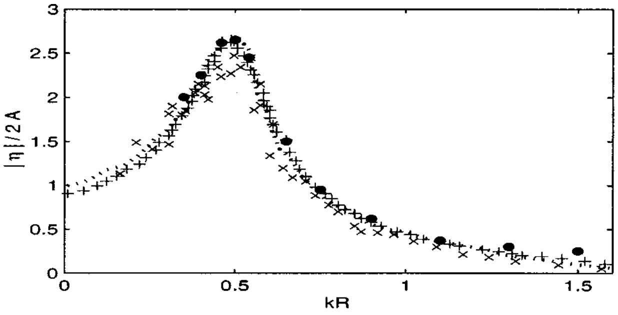

(a) Point P1

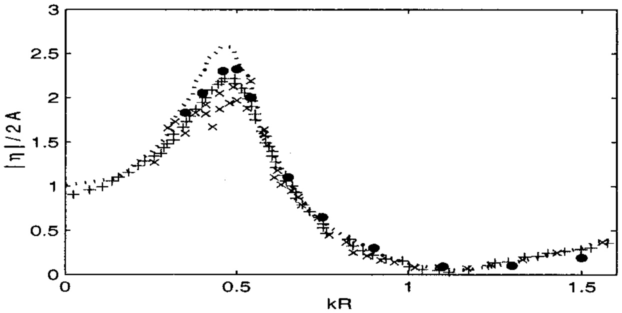

(a) Point P2

Fig. 8. Comparison of amplification factor at two points in a circular harbor: present numerical solution (●●●); Lee's (1971) experiment (×××); mild slope FEM (+++) (Jeong 1999); linear theoretical solution (· · ·)

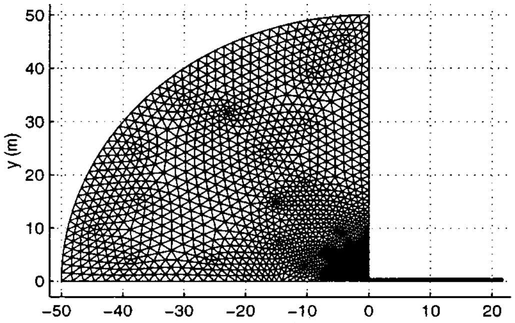

(a) Zoom-out view

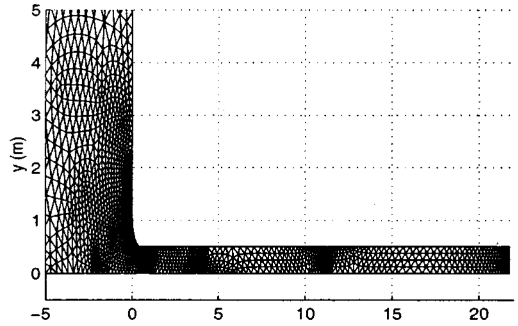

(b) Close-up view

Fig. 9. Finite-element mesh for Rogers and Mei's (1978) experiment

RM performed experiments for three bays of length 1.211, 4.173, and 7.136 ft, hereafter referred to as Bay 1, Bay 2, and Bay 3, respectively. Since the wave system was nonlinear, RM experimentally determined those bay lengths by producing the first three resonant peaks. The wavemaker, located at a distance of 31 ft from the bay mouth, generates waves with a wave period of 1.545 s. A constant water depth of 6 in. was used, and the corresponding wavelength was about 6 ft; three incident wave amplitudes were tested for each bay.

RM's physical experiments first measured the amplitude of the standing waves at the bay mouth with the bay completely closed. From these measurements the harmonic amplitudes and phase differences were calculated and used as the boundary condition for their numerical calculations for the wave field inside the bay. RM noted that in their theory and experiments the zeroth harmonic was assumed to be small and was removed from the Fourier analysis.

To compare the present numerical results with RM's experiments, we need to follow the experimental procedure exactly. However, the limitation of the computational resources makes it necessary to use a smaller domain and place the wavemaker much closer to the bay than in RM's experiments.

Fig. 9(a) shows the computational domain for Bay 3, whose shape is similar to the one shown in the previous section. Again, since the problem is symmetric with respect to the *y*-axis, only a half domain is used for computations. The physical dimensions of the rectangular bay are a width of 0.5 m, a length of 21.75 m, and a depth of 1.525 m. This represents a 1:10 prototype of RM's Bay 3 experimental setup. In Fig. 9(b), the automatic mesh generator causes the mesh refinement in some areas in a bay. To avoid the singular behavior at the corner of the harbor mouth, the edge of the bay mouth is rounded. It will later be shown that the numerical solution in the bay is only slightly affected by this modification of the bay mouth.

The center of the numerical internal wavemaker is located at $x=-18\,\mathrm{m}$, and the wavemaker source region is $(x,y)\in[-20,-16]\times[0,20]$ m. The target wave generated in the internal wavemaker is chosen in such a way that the harmonic amplitudes calculated at $(x,y)=(0,0)$ with the bay mouth closed are the same as RM's measurements. Two target wave components are found sufficient to reproduce RM's measurements: the first has a wave amplitude of 0.035 m and a wavelength of 18.3 m, with a corresponding wave period of 4.9 s; and the second has a wave amplitude of 0.01 m and a wavelength of 7.9 m, with a wave period of 2.45 s.

For the sponge layer, the center of the radiation is located at $\mathbf{x_c}=(0,0)$, and the starting position of the sponge layer is $\Gamma^S=180\,\mathrm{m}$. There are 3,825 nodes and 7,200 elements in the computational domain and around 4 elements across the bay, and the element size gradually increases toward the boundary Γ_W^E in the ocean. The size of the element near Γ_W^E is more than 10 times larger than the one near the harbor mouth.

Fig. 10 shows the overall view of the snapshots of free-surface elevation at different times for the case of Bay 3. Fig. 10(a) is at $t=15.2\,\mathrm{s}$, and the response of the bay has not been fully developed. As time goes on, certain natural frequencies of the bay are resonated, and the amplified surface elevation is clearly shown in Figs. 10(b–c). It is also evident that the sponge layer effectively damps out the reflected and radiated outgoing waves. Although the elementwise small oscillations, whose amplitude is less than 0.001 m, are generated at the harbor mouth, they do not affect the numerical solutions in time and space. There is no visible free-surface variation across the bay, which is consistent with RM's observation in the experiments.

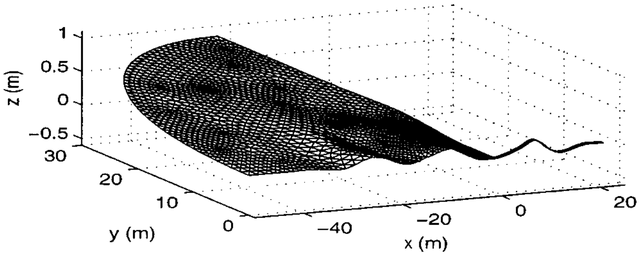

(a) t = 15.2 *sec*

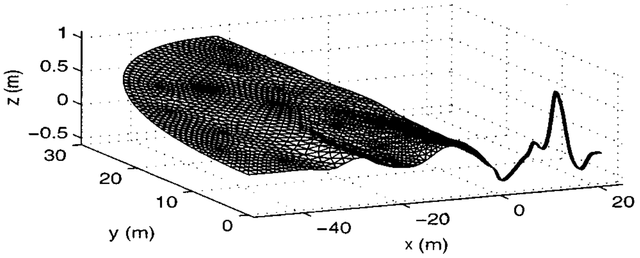

(b) t = 50.0 *sec*

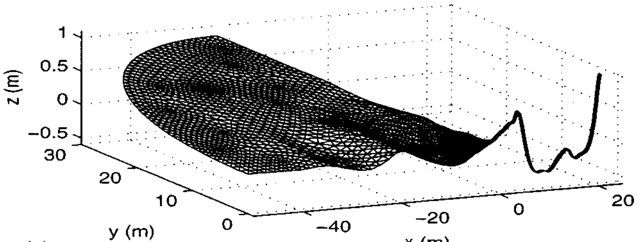

(c) t = 52.9 *sec*

Fig. 10. Snapshots of free-surface elevation for Rogers and Mei's (1978) experiment

To verify if the system has reached a quasi-steady state, the time history of free-surface elevation at different locations is plotted in the left panels in Fig. 11. The time series shows a quite different pattern of free surface movement at different locations. In front of the harbor entrance [$\mathbf{x}=(-4,0)$], the free-surface oscillation is very small for all time, indicating that there is a node. As shown in Figs. 11(b–e), the higher harmonic components start to emerge in the bay. Because of the standing-wavelike motions in the bay, each location reveals a different pattern of free-surface fluctuations. Figs. 11(b and d) show the antinodes for the first harmonic, while Figs. 11(c and e) demonstrate the nodes. These plots also show an initial modulation period before the system reaches a quasi-steady state, similar to the linear system in the previous section. These modulations are most obviously observed at the inner locations of the bay [Figs. 11(d and e)], and a quasi-steady state is reached at around $t=150$ s.

The characteristics of free-surface oscillations at different locations can also be revealed in terms of spectral components. The right panels of Fig. 11 show the amplitude spectra normalized by the water depth at the same location as the one in the left panels. Using the fast Fourier transform (FFT), the amplitude spectra are obtained for around 15 wave periods, $t\in[150,225]$ s. The first harmonic component corresponds to 0.2 Hz, which is very close to one of the incoming wave frequencies, and the second and third harmonic components are 0.4 and 0.6 Hz, respectively. As expected, near the harbor mouth, $\mathbf{x}=(-4,0)$, all harmonic components are very small. The spectra at $\mathbf{x}=(2.4,0)$ and $\mathbf{x}=(12.5,0)$ [Figs. 11(b and d)] represent the generation of higher harmonic components with the corresponding reduction in the magnitude of the first harmonic. On the other hand, Figs. 11(c and e) show that the magnitude of the higher harmonics is even larger than that of the first harmonic. Especially at $\mathbf{x}=(17.2,0)$ [Fig. 11(e)], the second harmonic amplitude is greatly amplified, which is in accord with RM's observation that the secondary resonance peak is developed through nonlinear interactions.

Note that the zeroth harmonic amplitude at certain locations is not entirely zero. The largest value is around 0.02, which occurs when the first harmonic is weak [Figs. 11(c and e)]. This magnitude of the zeroth harmonic is consistent with RM's theoretical argument—the order of magnitude of the zeroth harmonic$=O(\varepsilon^2)$—since the largest measured value of ε in RM's experiment is around 0.15 (Fig. 12), so that $O(\varepsilon^2)\sim 0.023$. A comparison of numerical results with experimental data is not available, since the zeroth harmonic has been removed from Fourier analysis in RM's experiments.

Fig. 12 compares the present results with RM's experimental data and theoretical solutions for Bay 3. The x-axis is normalized by $\sqrt{gh}/\omega$, and the harmonic amplitude is normalized by the water depth. A good agreement is observed between measured data and present numerical results. For the first harmonic, the existence of nodes and antinodes along the bay is demonstrated; for the second, the amplitude decreases gradually toward the bay entrance and is well captured by the present model, whereas RM's theory predicts a rather uniform amplitude along the bay. The energy transfer to the higher harmonics in the bay and the generation of a secondary resonant peak through the nonlinear interactions are shown clearly in the present case.

We remark here that the numerical results show short wave oscillations near the bay mouth for the second and third harmonic components. These wiggles are due mainly to the strong velocity of the gradients near the corner of the bay entrance. It is expected that a further rounding of the corner could reduce the intensity of the wiggles. Although the wiggles are quite small, they affect the convergence of the solution so that a rather large number of iterations (which sometimes reach 15–20) and a small time step ($T/\Delta t=100$) are needed to get a converged solution. Further research is necessary to resolve the singularity at the corner boundary and to achieve a fast convergence.

Fig. 13 shows the comparison for Bay 2. The numerical solutions for the first harmonic are almost identical to RM's theoretical results. Nodes and antinodes in the second and third harmonic are well represented by the numerical results. For the third harmonic, the spatial variation of the harmonic amplitude—decreasing from the bay end toward the middle of the bay and then increasing toward the bay entrance—are well simulated by the present numerical model. Unlike the previous case of Bay 3, the measured envelope of the second harmonic amplitudes in Bay 2 does not show any variation in space, which is also captured in the numerical results.

Near the bay entrance, the present numerical solutions overpredict the measured data, especially for the second harmonic. Similar overprediction near the bay mouth has been observed in Bay 3, which might be due to the fact that the entrance loss has not been incorporated into the present model.

The comparison for Bay 1, the shortest bay, is shown in Fig. 14. The overall agreement is quite good. The numerical solutions predict well the general pattern of amplitude variation of each harmonic in space. It is noted that for the first and second harmonic, the node outside the bay locates near $x'=x/h=-1$, regardless of the bay length. Therefore, the energy transfer between

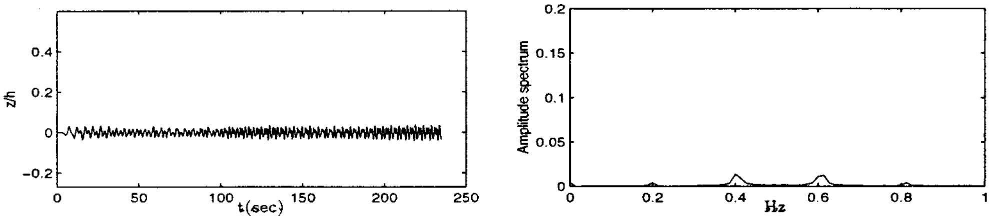

(a) x = -4.0 m

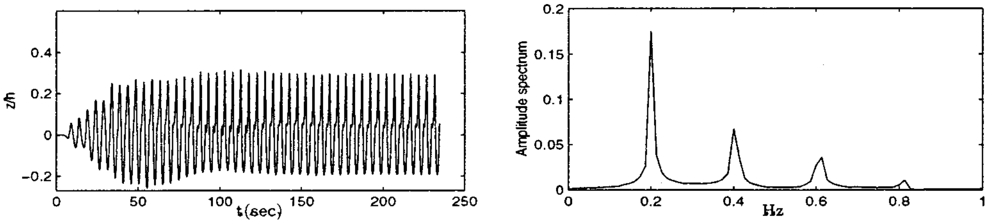

(b) $x = 2.4\ m$

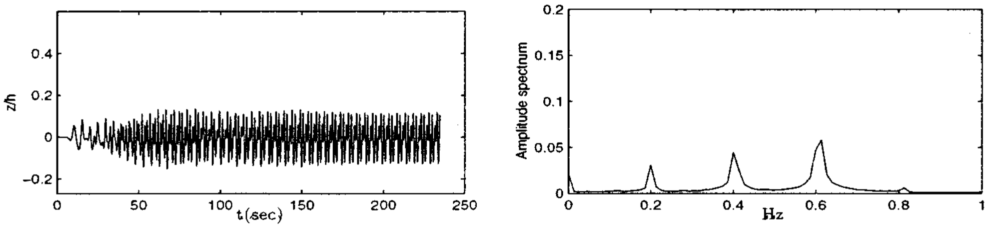

(c) $x = 7.6\ m$

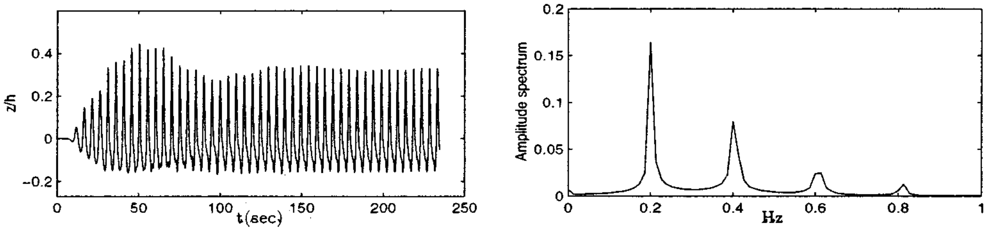

(d) $x = 12.5\ m$

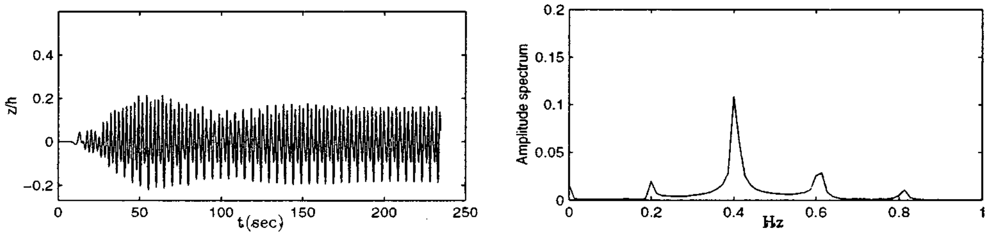

(e) $x = 17.2\ m$

Fig. 11. Time history of free surface elevation and amplitude spectrum at different locations along centerline of bay

the first and second harmonic components would be active up to this point.

Resonant Generation of Subharmonics

Harbor resonance can be caused by bound infragravity (subharmonic) waves (Bowers 1977; Mei and Agnon 1989; Wu and Liu 1990). Through interactions between bound infragravity waves and harbor structures, free infragravity waves can also be generated locally, and when the frequency of the infragravity waves coincides with the natural frequency of the harbor, a resonant excitation occurs.

In this section, the present model is used to study wave-group-induced harbor resonance. The incoming wave system generated by the internal wavemaker consists of two carrier wave components. A bound subharmonic wave is generated through the nonlinear interaction of carrier waves, and the frequency of the bound subharmonic wave is designed to be the same as the natural frequency of the harbor, so that the subharmonic wave component is expected to be resonated inside the bay.

The geometry of the longest rectangular bay used in RM's experiment (Bay 3) is chosen for this study. Fig. 15 shows the linear analytical solution of the amplification factor for this ge-

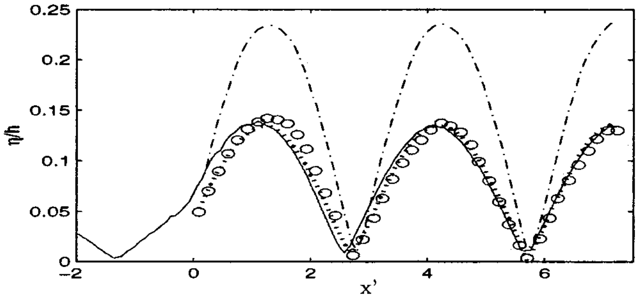

(a) First harmonic

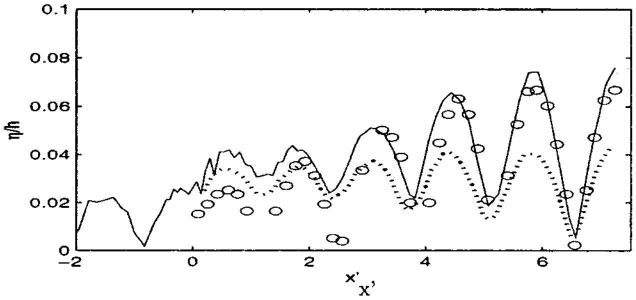

(b) Second harmonic

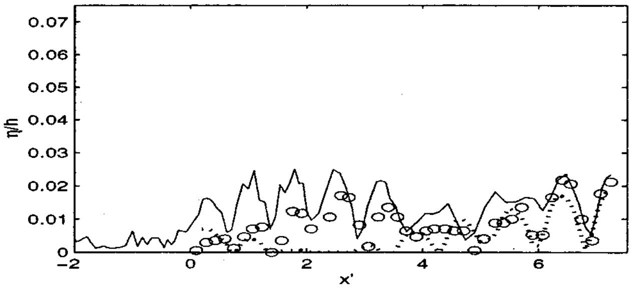

(c) Third harmonic

Fig. 12. Comparison of present numerical results with experimental data and Rogers and Mei's (1978) solutions for the longest bay (Bay 3): experimental data (○○○); present numerical solution (——); Rogers and Mei's nonlinear solution (· · ·); linear theoretical solution (—·—·—·—)

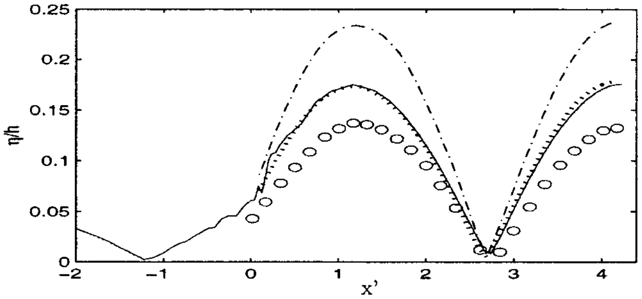

(a) First harmonic

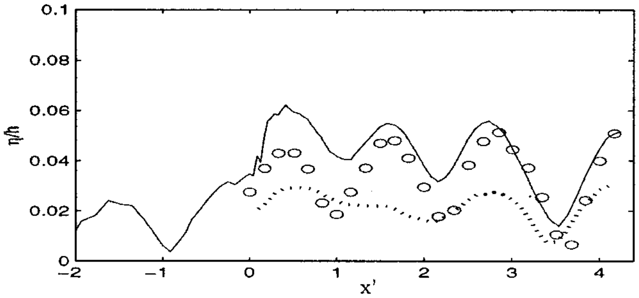

(b) Second harmonic

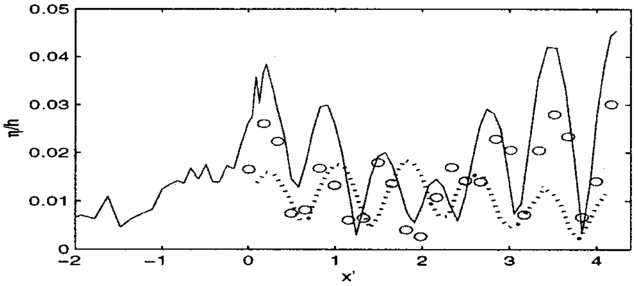

(c) Third harmonic

Fig. 13. Comparison of present numerical results with experimental data and Rogers and Mei's (1978) solutions for middle-length bay (Bay 2): experimental data (○○○); present numerical solution (——); Rogers and Mei's nonlinear solution (· · ·); linear theoretical solution (—·—·—·—)

ometry. As shown in the figure, ω_1, which corresponds to the third resonant mode, is very close to the incoming wave frequency studied in the previous section. In addition to ω_1, an additional component with frequency ω_2 is also generated in the internal wavemaker. The choice of ω_2 is made such that the bound subharmonic wave with a beat frequency $\Delta\omega = \omega_2 - \omega_1$ coincides with the frequency of the second resonant mode. The frequencies of the two carrier waves are $\omega_1 = 0.21$ and $\omega_2 = 0.33$ Hz, respectively; the same target wave amplitude is used, that is, $A_1 = A_2 = 0.05$ m, and the corresponding bound long-wave period is about 8 s.

The numerical results of this case show very complicated free-surface fluctuations. Due to the narrowness of the bay, no surface variation across the bay is observed. The temporal variation of the wave energy can be analyzed through a wavelet spectrum, as shown in Fig. 16. At $x = 2.4$ and 12.5 m [Figs. 16(a and c)], the wave energy is concentrated at the carrier wave period (4–6 s), and the energy level at the subharmonic wave (8 s) is low. Note that one of the incoming carrier waves, whose period is 4.8 s, coincides with the third resonant mode in the bay so that the energy level at 4–6 s is amplified and is much bigger than the one for the other incoming wave, whose period is 3 s.

As expected, the subharmonic wave energy does indeed dominate at certain locations, as shown in Figs. 16(b and d), and at the end of the bay [Fig. 16(e)], the dominant energy level at both the carrier wave and subharmonic wave is shown clearly. Comparing the time for the subharmonic wave energy to fully emerge at different locations [Figs. 16(b, d, and e)], shows that the further the wave's position from the bay mouth, the more time it takes to emerge. This seems reasonable because time and space are required to transfer wave energy into subharmonics. Once the subharmonic waves are fully developed, they stay in the bay, but short wave components whose wave period is less than 3 s have not reached a quasi-steady state at any location. This phenomenon may be explained by the relatively intensive energy transfer between higher harmonic wave components. On the other hand, it is interesting to see the periodic feature of the wave energy transfer between long wave components whose period is more than 6 s, as

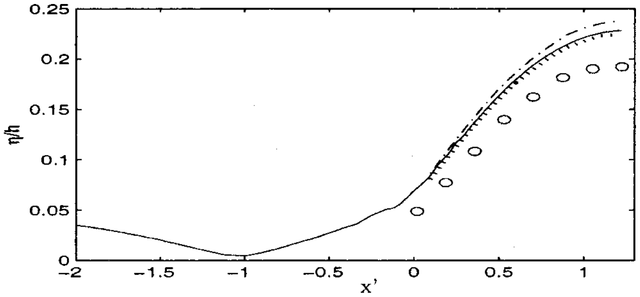

(a) First harmonic

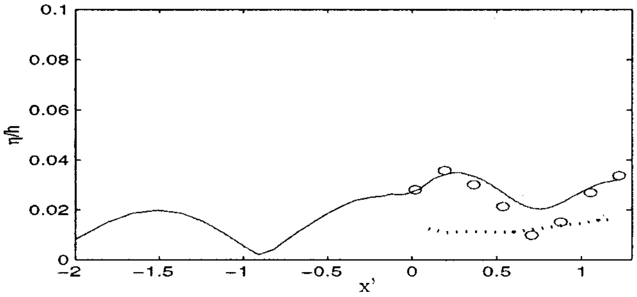

(b) Second harmonic

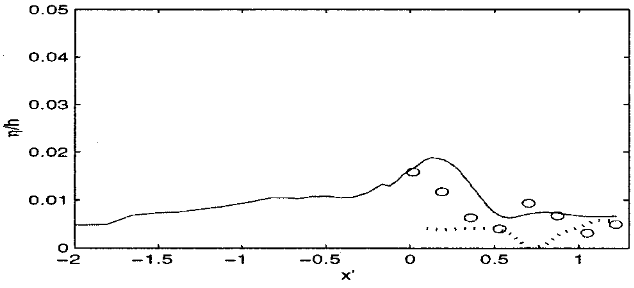

(c) Third harmonic

Fig. 14. Comparison of present numerical results with experimental data and Rogers and Mei's (1978) solutions for shortest bay (Bay 1): experimental data (○○○); present numerical solution (——); Rogers and Mei's nonlinear solution (· · ·); linear theoretical solution (—·—·—·—)

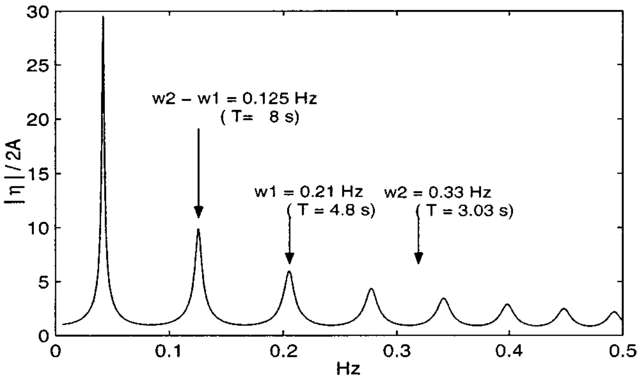

Fig. 15. Analytic solution of amplification factor for longest bay used in Rogers and Mei's (1978) experiment

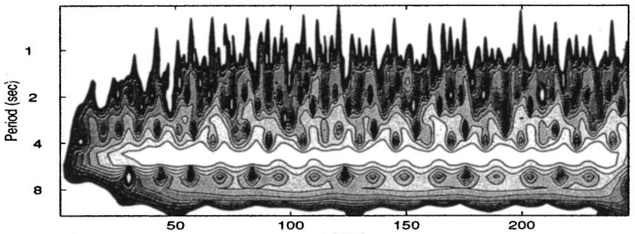

(a) $x = 2.4\ m$

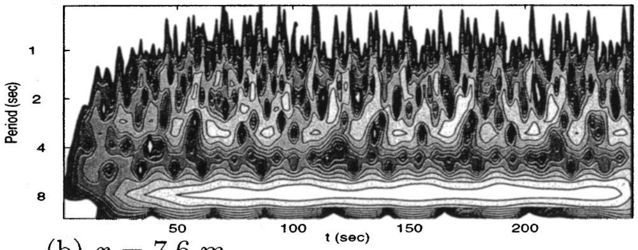

(b) $x = 7.6\ m$

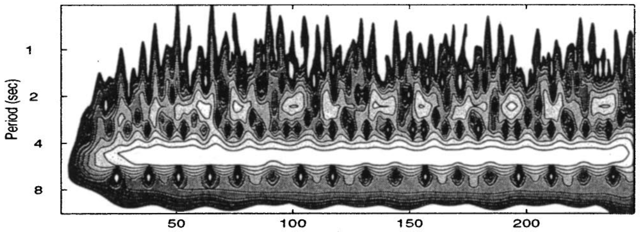

(c) $x = 12.5\ m$

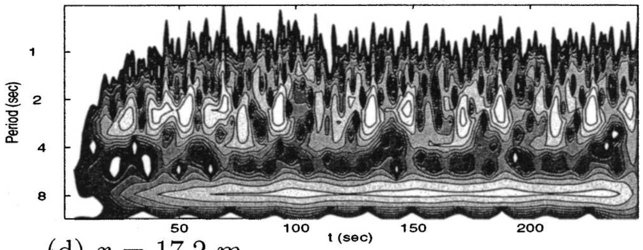

(d) $x = 17.2\ m$

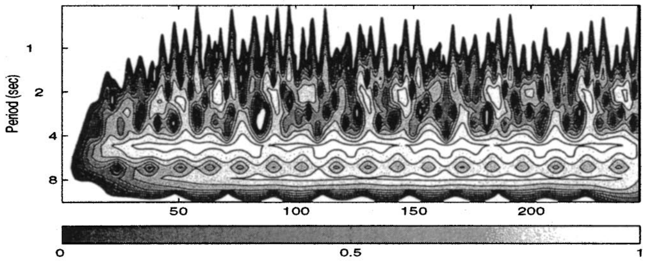

(e) $x = 21.7\ m$

Fig. 16. Time history and wavelet spectrum at different location along centerline of bay

shown in almost all locations. Among all of them, the nearly 12 s periodic feature at the innermost bay [Fig. 16(e)] is the most obviously shown.

Using the time series of free-surface elevations, FFT analysis is performed to obtain the amplification factor, as shown in Fig. 17. The time segment of 150 to 250 s is used in the FFT, since the carrier wave and subharmonic waves have reached a quasi-steady state at around 70 s, as shown in Fig. 16. Fig. 17(a) shows the amplification factor at the bay entrance [$\mathbf{x}=(0,0)$] with the bay

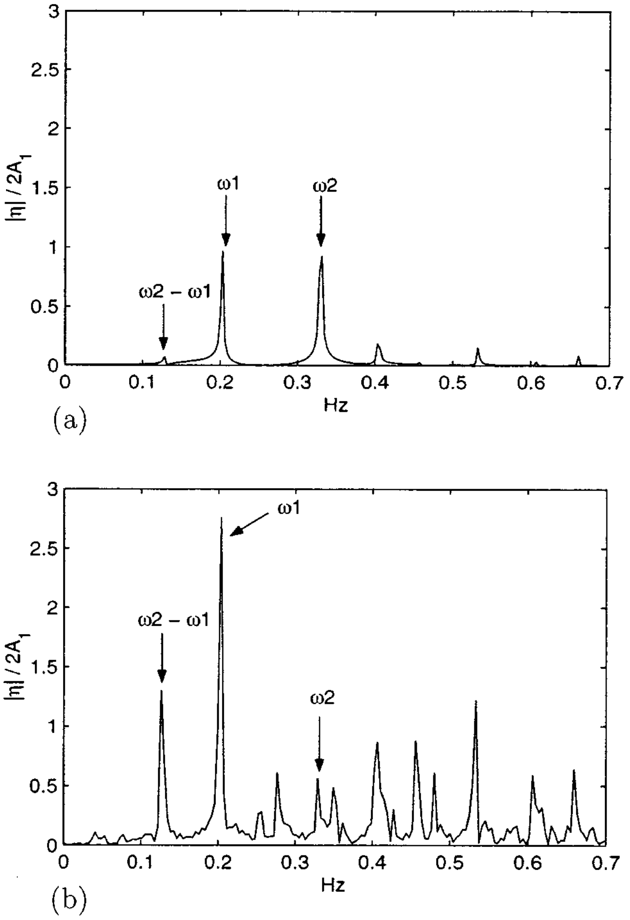

Fig. 17. Amplification factor: (a) at bay entrance with bay closed; (b) at end of open bay

closed. Note that only one target wave height $(2A_1)$ is used for normalization so that two carrier waves have an amplification factor of almost 1. Since the nonlinearity is not strong $(\varepsilon=0.13)$, the amplification factors for subharmonics and superharmonics are not large. However, when the bay is opened, the subharmonic wave component is clearly amplified, since its frequency coincides with the second resonant mode of the bay [Fig. 17(b)].

The spatial amplitude variations along the bay for a carrier incoming wave and subharmonic wave are shown in Fig. 18. The pattern of spatial variation of the subharmonic wave amplitude is very similar to the carrier wave response to the second resonant mode, as shown in Fig. 13(a), which indicates a spatial variation of amplification for a subharmonic wave whose wave energy is supplied from superharmonic waves.

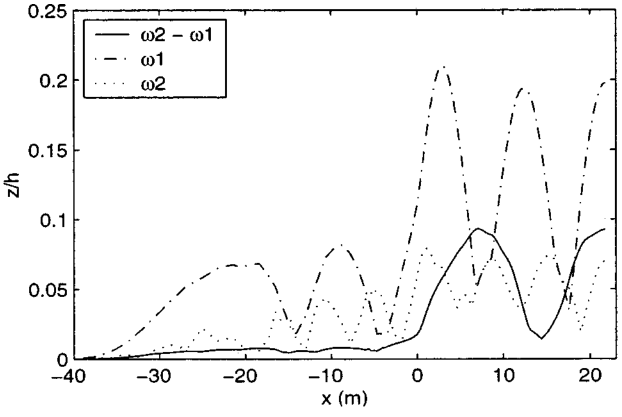

Fig. 18. Spatial variation of amplification factor along bay

Concluding Remarks

The newly developed finite-element model based on modified Boussinesq equations is applied to linear and nonlinear harbor oscillation problems. An internal wavemaker is employed, and the reflected/radiated waves are absorbed in the sponge layer. Several comparisons between the present model and the experimental data are presented to demonstrate the applicability of the present model for studying and analyzing nonlinear harbor resonance problems.

To enable the present model to be used for more practical applications, the computational efficiency needs to be improved. To avoid the singular behavior at the sharp edge of the harbor mouth, the boundary has been smoothed and a fine mesh is used in the present work. This approach may not be practical for a large-scale problem with a very complex boundary. Further investigation needs to be performed to improve the convergence characteristics near the sharp corner. Furthermore, different dissipation mechanisms, such as wavebreaking, bottom friction, and partial reflection, need to be added to the present model.

Acknowledgments

This research has been supported by research grants from the National Science Foundation (BES9714182 and CMS9908392) to Cornell University, the National Taiwan University, Taiwan, and the National Research Laboratory Program (Coastal Engineering Laboratory, Hanyang University), Korea.

References

Bowers, E. C. (1977). "Harbor resonance due to set-down beneath wave groups." *J. Fluid Mech.*, 79, 71–92.

Chen, H. S., and Mei, C. C. (1974). "Oscillations and wave forces in an offshore harbor." *Rep. No. 190*, Dept. of Civil Engineering, Massachusetts Institute of Technology, Cambridge, Mass.

Ippen, A. T., and Goda, Y. (1963). "Wave induced oscillations in harbor: The solution for a rectangular harbor connected to the open-sea." *Rep. No. 59*, Dept. of Civil Engineering, Massachusetts Institute of Technology, Cambridge, Mass.

Jeong, W. M. (1999). "Field study and finite element analysis of harbor oscillations." PhD thesis, Seoul National Univ., Seoul, Korea.

Lee, J. J. (1971). "Wave-induced oscillations in harbors of arbitrary geometry." *J. Fluid Mech.*, 45, 375–394.

Lepelletier, T. G. (1980). "Tsunamis—Harbor oscillations induced by nonlinear transient long waves." *W. M. Keck Laboratory Rep. No. KH-R-41*, California Institute of Technology, Pasadena, Calif.

Lepelletier, T. G., and Raichlen, F. (1987). "Harbor oscillations induced by nonlinear transient long waves." *J. Waterw., Port, Coastal, Ocean Eng.*, 113(4), 381–400.

Li, Y. S., Liu, S.-X., Yu, Y.-X., and Lai, G.-Z. (1999). "Numerical modeling of Boussinesq equations by finite element method." *Coastal Eng.*, 37, 97–122.

Lillycrop, L. S., Briggs, M. J., Harkins, G. S., Boc, S. J., and Okihiro, M. S. (1993). "Barbers Point Harbor, Oahu, Hawaii, monitoring study." *Technical Rep. CERC-93-18*, U.S. Army Engineers Waterways Experiment Station, Vicksburg, Miss.

Mei, C. C., and Agnon, Y. (1989). "Long-period oscillations in a harbour induced by incident short waves.'' *J. Fluid Mech.*, 208, 595–608.

Nwogu, O. (1993). ''Alternative form of Boussinesq equations for nearshore wave propagation.'' *J. Waterw., Port, Coastal, Ocean Eng.*, 119(6), 618–638.

Panchang, V. G., Chen, W., Xu, B., Schlenker, K., Demirbilek, Z., and Okihiro, M. (2000). ''Exterior bathymetric effects in elliptic harbor wave models.'' *J. Waterw., Port, Coastal, Ocean Eng.*, 126(2), 71–78.

Rogers, S. R., and Mei, C. C. (1978). ''Nonlinear resonant excitation of a long and narrow bay.'' *J. Fluid Mech.*, 88, 161–180.

Tsay, T. K., and Liu, P. L.-F. (1983). ''A finite element model for wave refraction and reflection.'' *Appl. Ocean. Res.*, 5(1), 30–37.

Walkley, M., and Berzins, M. (2002). ''A finite element method for the two-dimensional extended Boussinesq equations.'' *Int. J. Numer. Methods Fluids*, 39, 865–885.

Wei, G., and Kirby, J. T. (1995). ''Time-dependent numerical code for extended Boussinesq equations.'' *J. Waterw., Port, Coastal, Ocean Eng.*, 121(5), 251–261.

Wei, G., Kirby, J. T., and Sinha, A. (1999). ''Generation of waves in Boussinesq models using a source function method.'' *Coastal Eng.*, 36, 271–299.

Woo, S.-B., and Liu, P. L.-F. (2004). ''Finite-element model for modified Boussinesq equations. I: Model development.'' *J. Waterw., Port, Coastal, Ocean Eng.*, 130(1), 1–16.

Wu, J.-K., and Liu, P. L.-F. (1990). ''Harbor excitations by incident wave groups.'' *J. Fluid Mech.*, 217, 595–613.

Xu, B., Panchang, V., and Demirbilek, Z. (1996). ''Exterior reflections in elliptic harbor wave models.'' *J. Waterw., Port, Coastal, Ocean Eng.*, 122(3), 118–126.